

# ChemComm

Chemical Communications

Accepted Manuscript

This article can be cited before page numbers have been issued, to do this please use: I. Vamvasakis, A. Grammenos and G. S. Armatas, *Chem. Commun.*, 2026, DOI: 10.1039/D6CC01893A.



This is an Accepted Manuscript, which has been through the Royal Society of Chemistry peer review process and has been accepted for publication.

Accepted Manuscripts are published online shortly after acceptance, before technical editing, formatting and proof reading. Using this free service, authors can make their results available to the community, in citable form, before we publish the edited article. We will replace this Accepted Manuscript with the edited and formatted Advance Article as soon as it is available.

You can find more information about Accepted Manuscripts in the [Information for Authors](#).

Please note that technical editing may introduce minor changes to the text and/or graphics, which may alter content. The journal's standard [Terms & Conditions](#) and the [Ethical guidelines](#) still apply. In no event shall the Royal Society of Chemistry be held responsible for any errors or omissions in this Accepted Manuscript or any consequences arising from the use of any information it contains.

## COMMUNICATION

Reversing the Activity Landscape of MoS<sub>x</sub> Electrocatalysts via Ni<sub>x</sub>P Interfacial Coupling for Alkaline Hydrogen EvolutionIoannis Vamvasakis,<sup>\*a</sup> Aggelos Grammenos<sup>b</sup> and Gerasimos S. Armatas<sup>\*a</sup>Received 00th January 20xx,  
Accepted 00th January 20xx

DOI: 10.1039/x0xx00000x

**Interfacial coupling offers a powerful route to modulate electrochemical kinetics, yet its interplay with catalyst morphology remains unclear. Here, Ni<sub>x</sub>P coupling reshapes the activity landscape of MoS<sub>x</sub>, enabling a highly active amorphous interface for alkaline HER. Operando electrochemical analysis reveals a shift beyond Volmer-limited kinetics via enhanced charge transfer and hydrogen adsorption.**

Green hydrogen production via alkaline water electrolysis is central to the sustainable energy systems. However, the hydrogen evolution reaction (HER) remains intrinsically sluggish in alkaline media primarily due to the additional energy barrier associated with water dissociation.<sup>1–5</sup> Although Pt-based catalysts exhibit near-optimal HER activity, their scarcity and cost necessitates the development of efficient earth-abundant alternatives.<sup>6,7</sup> Among these, molybdenum sulfides (MoS<sub>x</sub>) have attracted considerable attention owing to their favourable hydrogen adsorption energetics, chemical stability, and structural tunability.<sup>8–14</sup> Nevertheless, their catalytic performance is highly governed by crystallinity and morphology, as active sites are predominantly located at edges and defect-rich domains, while the basal planes are largely inert.<sup>14–17</sup> Consequently, substantial efforts have been devoted on phase engineering,<sup>10,17</sup> nanostructuring,<sup>12,16,17</sup> and defect modulation<sup>18–20</sup> to increase active-site exposure and improve charge-transfer kinetics.

Beyond intrinsic structural optimization, interfacial engineering has emerged as an effective strategy to modulate catalytic activity through electronic coupling between dissimilar phases.<sup>21–25</sup> In this context, nickel phosphides (Ni<sub>x</sub>P), particularly amorphous Ni–P phases, are attractive components for hybrid HER catalysts due to their metallic conductivity and favourable hydrogen adsorption energetics.<sup>26–28</sup> Electrodeposition enables precise control over the formation of conformal Ni<sub>x</sub>P overlayers on wide range of sulfide substrates, offering a versatile

platform for constructing hybrid electrocatalysts.<sup>29–33</sup> Despite these advantages, the interplay between MoS<sub>x</sub> crystallinity and Ni<sub>x</sub>P interfacial coupling in governing alkaline HER kinetics remains poorly understood.

Herein, we show that Ni<sub>x</sub>P surface modification not only enhances HER activity but fundamentally reshapes the morphology-activity relationship in MoS<sub>x</sub> electrocatalysts. Strikingly, Ni<sub>x</sub>P coupling inverts the intrinsic activity trend, rendering the amorphous Ni<sub>x</sub>P/MoS<sub>x</sub> interface the most active configuration. Operando electrochemical analysis, combined with kinetic isotope measurements, reveal that interfacial electronic coupling simultaneously accelerates charge-transfer and hydrogen adsorption kinetics, driving a transition beyond the Volmer-limited regime.

Three distinct MoS<sub>x</sub> architectures were synthesized on carbon cloth (CC): (i) amorphous electrodeposited MoS<sub>x</sub>, (ii) thermally annealed MoS<sub>x</sub> at 800 °C (MoS<sub>x</sub>-800), exhibiting enhanced crystallinity and preferential base-plane orientation, and (iii) hydrothermally grown MoS<sub>x</sub> nanosheets (MoS<sub>x</sub>-hydro). Subsequent galvanostatic deposition of amorphous Ni<sub>x</sub>P yielded the corresponding Ni<sub>x</sub>P/MoS<sub>x</sub>, Ni<sub>x</sub>P/MoS<sub>x</sub>-800, and Ni<sub>x</sub>P/MoS<sub>x</sub>-hydro heterostructures (**Fig. S1**). Scanning electron microscopy (SEM) reveals pronounced morphology-dependent differences prior and following Ni<sub>x</sub>P deposition. The electrodeposited MoS<sub>x</sub> exhibits a smooth, conformal coating (**Fig. S2a-c**), whereas MoS<sub>x</sub>-800 shows a denser morphology (**Fig. S2d-f**), consistent with thermally induced densification. In contrast, MoS<sub>x</sub>-hydro presents a rough, interconnected nanosheet network (**Fig. S2g-i**), indicative of an edge-rich structure. After Ni<sub>x</sub>P deposition, the overlayer growth is strongly dictated by the underlying MoS<sub>x</sub> morphology. On amorphous MoS<sub>x</sub>, Ni<sub>x</sub>P forms a conformal nanoparticulate overlayer (**Fig. 1a**), whereas MoS<sub>x</sub>-800 yields a dense, featureless Ni<sub>x</sub>P layer (**Fig. S3a-b**), consistent with particle coalescence and limited nucleation heterogeneity. For MoS<sub>x</sub>-hydro, the nanosheet architecture is preserved, with Ni<sub>x</sub>P nanoparticles uniformly decorating the hierarchical structure (**Fig. S3c-d**). These observations indicate that Ni<sub>x</sub>P nucleation and growth are governed by the local surface structure of MoS<sub>x</sub>,

<sup>a</sup> Department of Materials Science and Engineering, University of Crete, Vassilika Vouton, Heraklion 70013, Greece.

<sup>b</sup> Department of Chemistry, University of Crete, Vassilika Vouton, Heraklion 70013, Greece.



resulting in a morphology-dependent interfacial assembly. Energy dispersive X-ray spectroscopy (EDS, **Table S1**) shows that electrodeposited  $\text{MoS}_x$  is slightly sulfur-deficient ( $\text{Mo}:\text{S} \approx 1:1.4$ ), whereas both  $\text{MoS}_x$ -800 and  $\text{MoS}_x$ -hydro exhibit a stoichiometric  $\text{MoS}_2$  composition. Upon  $\text{Ni}_x\text{P}$  deposition, a Ni-rich surface layer ( $\text{Ni}:\text{P} \approx 11\text{--}14:1$ ) dominates the detected composition, accompanied by attenuation of Mo and S signals due to overlayer screening effects. Notably, the Mo:S ratios remain unchanged relative to the pristine samples, indicating preservation of the underlying  $\text{MoS}_x$  framework during heterostructure formation. Elemental mapping further corroborates the layered architecture, with Ni and P localized at the surface and Mo and S confined to the substrate (**Fig. 1b**).

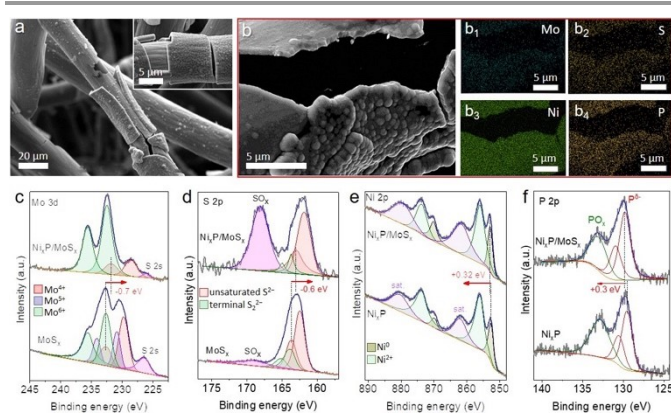


**Fig. 1.** (a) Representative SEM images of as-synthesized  $\text{Ni}_x\text{P}/\text{MoS}_x$ . (b) Corresponding EDS elemental mapping showing the spatial distribution of Mo, S, Ni and P. (c, d) High-resolution XPS spectra of Mo 3d and S 2p for pristine  $\text{MoS}_x$  and  $\text{Ni}_x\text{P}/\text{MoS}_x$ . (e, f) High-resolution XPS spectra of Ni 2p and P 2p for  $\text{Ni}_x\text{P}$  and  $\text{Ni}_x\text{P}/\text{MoS}_x$ .

X-ray diffraction (XRD) was employed to assess the crystallinity of the synthesized materials. Electrodeposited  $\text{MoS}_x$  exhibits no discernible reflections, consistent with an X-ray amorphous structure. In contrast,  $\text{MoS}_x$ -hydro displays broad (002), (100), and (110) reflection characteristic of nanocrystalline 2H- $\text{MoS}_2$  (PDF #37-1492; space group  $P6_3/mmc$ ) (**Fig. S4**). Notably,  $\text{MoS}_x$ -800 shows a pronounced (002) peak, indicative of enhanced crystallinity and preferential basal-plane orientation parallel to the substrate.<sup>34,35</sup> This structural evolution reflects a transition from a disordered edge-rich structure to a more ordered basal-plane-dominated configuration. Following  $\text{Ni}_x\text{P}$  deposition, all heterostructures exhibit a broad diffraction feature at  $2\theta \approx 44^\circ$  (**Fig. S5**), which is characteristic of a quasi-amorphous  $\text{Ni}_x\text{P}$  phase. In contrast, Ni-only control samples display sharp reflections corresponding to crystalline metallic Ni, confirming that phosphorous incorporation induces amorphization into a Ni–P phase. Raman spectroscopy provides complementary insight into the local structure. All pristine  $\text{MoS}_x$  samples exhibit the characteristic in-plane  $E_{12g}$  and out-of-plane  $A_{1g}$  modes of  $\text{MoS}_2$  at  $\approx 383$  and  $\approx 407$   $\text{cm}^{-1}$ , respectively (**Fig. S6**). Among them,  $\text{MoS}_x$ -800 shows sharper and more intense features, consistent with increased crystallinity, whereas  $\text{MoS}_x$  and  $\text{MoS}_x$ -hydro display broader bands indicative of structural disorder and reduced domain size. Notably, enhanced low-wavenumber modes (145–240  $\text{cm}^{-1}$ ) are observed for  $\text{MoS}_x$  and  $\text{MoS}_x$ -hydro, which are attributed to edge-rich or defective

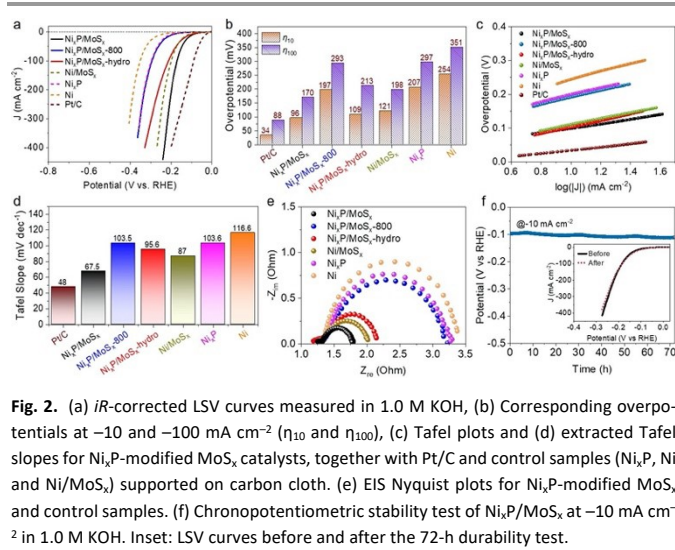
$\text{MoS}_2$  domains<sup>36–38</sup>, in agreement with XRD. After  $\text{Ni}_x\text{P}$  deposition, all heterostructures show broadened Raman peaks (**Fig. S7**), consistent with disordered metal-metalloid bonding in amorphous  $\text{Ni}_x\text{P}$ .<sup>39,40</sup> In contrast, Ni-only control samples display distinct Ni–O vibrational modes that are absent in  $\text{Ni}_x\text{P}$ -containing samples, indicating improved resistance of the  $\text{Ni}_x\text{P}$  overlayer to surface oxidation.

X-ray photoelectron spectroscopy (XPS) was conducted to probe the chemical states and interfacial electronic interactions. The Mo 3d spectrum of pristine  $\text{MoS}_x$  can be deconvoluted into  $\text{Mo}^{4+}$ ,  $\text{Mo}^{5+}$  and  $\text{Mo}^{6+}$  components (**Fig. 1c**), where  $\text{Mo}^{5+}$  species are associated with sulfur vacancies and non-stoichiometric environments characteristic of defective  $\text{MoS}_x$ .<sup>41</sup> Upon  $\text{Ni}_x\text{P}$  deposition, the  $\text{Mo}^{5+}$  contribution is markedly suppressed, leaving predominantly  $\text{Mo}^{4+}$  and  $\text{Mo}^{6+}$  states. This evolution indicates a modification of the local electronic structure, arising from interfacial charge redistribution between  $\text{Ni}_x\text{P}$  and  $\text{MoS}_x$ . The S 2p spectra comprise contributions from unsaturated  $\text{S}^{2-}$  and terminal  $\text{S}_2^{2-}$  species,<sup>42</sup> along with minor  $\text{SO}_x$  components arising from inevitable surface oxidation (**Fig. 1d**). The Ni 2p and P 2p spectra confirm the formation of a semi-metallic Ni–P phase composed of metallic Ni and low-valent  $\text{P}^{\delta-}$  species, with minor oxidized surface contributions (**Fig. 1e,f**). Importantly, systematic binding energy shifts are observed upon heterostructure formation. The Mo 3d and S 2p peaks shift to lower binding energies ( $\approx 0.6\text{--}0.7$  eV), whereas the Ni 2p and P 2p peaks shift to higher binding energies ( $\approx 0.3$  eV) relative to their respective references (pure  $\text{MoS}_x$  and  $\text{Ni}_x\text{P}$ ). This opposite shift indicates electron transfer from  $\text{Ni}_x\text{P}$  to  $\text{MoS}_x$ , providing clear evidence of strong interfacial electronic coupling. Such charge redistribution is expected to optimize hydrogen adsorption energetics and facilitate interfacial charge transfer during the HER. Full XPS peak assignments are summarized in **Table S2**.

The HER performance of the as-prepared electrodes was evaluated in 1.0 M KOH using a standard three-electrode configuration. Linear sweep voltammetry (LSV) was employed to determine the  $iR$ -corrected overpotentials at  $-10$  and  $-100$   $\text{mA cm}^{-2}$  ( $\eta_{10}$  and  $\eta_{100}$ ), which serve as key activity benchmarks. Among the pristine  $\text{MoS}_x$  samples (**Fig. S8a,b**),  $\text{MoS}_x$ -hydro exhibits the highest activity ( $\eta_{10} = 187$  mV;  $\eta_{100} = 312$  mV), followed by amorphous  $\text{MoS}_x$  ( $\eta_{10} = 240$  mV;  $\eta_{100} = 340$  mV), whereas  $\text{MoS}_x$ -800 shows the lowest activity ( $\eta_{10} = 314$  mV;  $\eta_{100} = 439$  mV). This trend correlates with the progressive decrease in exposed edge sites when transitioning from nanosheet-rich to basal-plane-dominated structures, highlighting the critical role of intrinsic active-site density in pristine  $\text{MoS}_x$  catalysts. Upon  $\text{Ni}_x\text{P}$  modification, however, a pronounced reordering of the activity trend is observed. Notably,  $\text{Ni}_x\text{P}/\text{MoS}_x$  requires overpotentials of only 96 and 170 mV to reach  $-10$  and  $-100$   $\text{mA cm}^{-2}$ , respectively, outperforming all other heterostructures and approaching the performance of Pt/C at high current densities (**Fig. 2a,b**). This inversion of the intrinsic activity sequence indicates that interfacial electronic coupling, rather than morphology alone, governs HER performance. In contrast,  $\text{Ni}_x\text{P}/\text{MoS}_x$ -hydro exhibits only moderate improvement ( $\eta_{10} = 109$  mV;  $\eta_{100} = 213$  mV), while  $\text{Ni}_x\text{P}/\text{MoS}_x$ -800 performs comparably to bare  $\text{Ni}_x\text{P}$  (**Fig. 2a,b**), suggesting a limited synergistic



contribution of the highly crystalline MoS<sub>2</sub> support to the overall catalytic performance. Control experiments using Ni-only and Ni/MoS<sub>x</sub> electrodes show significantly inferior activity (Fig. 2a,b), highlighting the critical role of phosphorus incorporation in modulating catalytic behavior. Furthermore, bare carbon cloth exhibits negligible activity (Fig. S8a), confirming that the observed catalytic response originates exclusively from the deposited active phases. Collectively, these results demonstrate that optimal HER performance is achieved at the amorphous-amorphous Ni<sub>x</sub>P/MoS<sub>x</sub> interface, emphasizing the importance of interfacial compatibility and strong electronic coupling. Notably, the performance of Ni<sub>x</sub>P/MoS<sub>x</sub> ranks among the highest reported for Ni–P-modified MoS<sub>2</sub>-based electrocatalysts (Table S3).



Further mechanistic insight was obtained from Tafel analysis in the low-overpotential region, electrochemical impedance spectroscopy (EIS), and electrochemically active surface area (ECSA) measurements. Pristine MoS<sub>x</sub> catalysts exhibit Tafel slopes of ≈98–136 mV dec<sup>-1</sup> (Fig. S8c,d), consistent with Volmer-limited HER kinetics, where water dissociation constitutes the rate-determining step. Most Ni<sub>x</sub>P- and Ni-modified samples retain similar behavior (Fig. 2c,d), including Ni<sub>x</sub>P/MoS<sub>x</sub>-800 (103.5 mV dec<sup>-1</sup>), Ni<sub>x</sub>P/MoS<sub>x</sub>-hydro (95.6 mV dec<sup>-1</sup>), as well as Ni<sub>x</sub>P, Ni, and Ni/MoS<sub>x</sub> control catalysts (≈87–116.6 mV dec<sup>-1</sup>), indicating that the Volmer step remains kinetically limiting in these systems. In contrast, Ni<sub>x</sub>P/MoS<sub>x</sub> exhibits a markedly reduced Tafel slope of 67.5 mV dec<sup>-1</sup>, indicative of a transition toward mixed Volmer-Heyrovsky kinetics with accelerated hydrogen evolution rates, approaching those of Pt/C (48 mV dec<sup>-1</sup>). This kinetic shift suggests that the Ni<sub>x</sub>P/MoS<sub>x</sub> interface lowers the barrier for hydrogen adsorption and electrochemical desorption, thereby altering the rate-determining step. EIS measurements provide complementary evidence for this mechanistic evolution. Among pristine samples, MoS<sub>x</sub>-hydro exhibits the lowest charge-transfer resistance (R<sub>ct</sub>), as reflected by the smaller semicircle in Nyquist plots (Fig. S9), consistent with its superior intrinsic activity. Following Ni<sub>x</sub>P deposition, however, Ni<sub>x</sub>P/MoS<sub>x</sub> displays the smallest semicircle diameter among all

catalysts (Fig. 2e), corresponding to the lowest interfacial R<sub>ct</sub> and most efficient charge transfer across the MoS<sub>x</sub>/Ni<sub>x</sub>P interface. In contrast, Ni<sub>x</sub>P/MoS<sub>x</sub>-hydro and Ni<sub>x</sub>P/MoS<sub>x</sub>-800 exhibit higher R<sub>ct</sub>, while Ni<sub>x</sub>P, Ni, and Ni/MoS<sub>x</sub> control samples show significantly poorer charge-transfer characteristics. These results indicate that interfacial electronic coupling, rather than intrinsic conductivity alone, governs the charge-transfer kinetics in these heterostructures. ECSA analysis further reveals a clear decoupling between surface area and catalytic activity. For pristine MoS<sub>x</sub>, the ECSA follows the trend MoS<sub>x</sub>-hydro (≈366 cm<sup>2</sup>) > MoS<sub>x</sub> (≈62 cm<sup>2</sup>) > MoS<sub>x</sub>-800 (≈29 cm<sup>2</sup>), consistent with their HER activity (Fig. S10). However, this correlation breaks down upon Ni<sub>x</sub>P modification (Fig. S11). Despite exhibiting the highest ECSA (≈551 cm<sup>2</sup>), Ni<sub>x</sub>P/MoS<sub>x</sub>-hydro does not deliver the best performance. Instead, Ni<sub>x</sub>P/MoS<sub>x</sub> achieves the highest activity with a comparatively modest ECSA (≈75 cm<sup>2</sup>), while other samples with similar or larger surface areas (≈61–122 cm<sup>2</sup>) remain less active. These findings demonstrate that HER activity is not governed by surface area alone but is instead dictated by interfacial charge-transfer kinetics. The amorphous Ni<sub>x</sub>P/MoS<sub>x</sub> interface uniquely optimizes hydrogen adsorption energetics and electron transfer, thereby overcoming the kinetic limitations associated with water dissociation.

The Ni<sub>x</sub>P/MoS<sub>x</sub> catalyst also exhibits excellent durability, retaining ≈87% of its initial activity after 72 h of continuous operation at -10 mA cm<sup>-2</sup> (Fig. 2f). Notably, the catalyst maintains, and slightly improves, its HER performance upon reuse (η<sub>10</sub> = 89 mV; η<sub>100</sub> = 169 mV, Fig. 2f, inset), suggesting the formation of a stable and catalytically optimized interface under operating conditions. Post-catalysis characterization reveals no significant structural degradation but indicates limited surface reconstruction. XRD patterns remain unchanged (Fig. S12a), confirming preservation of the bulk phase, while Raman spectra show the emergence of weak Ni–O features (Fig. S12b), indicative of minor surface oxidation. EDS analysis reveals a shift in the Mo:S ratio toward the stoichiometric 1:2 value (Table S1), consistent with increased MoS<sub>2</sub>-like ordering. XPS results (Fig. S13) confirm the predominance of Mo<sup>4+</sup> species, along with partial oxidation of S and Ni. Importantly, the Ni:P ratio remains essentially unchanged (≈14:1; Table S1), indicating retention of the Ni–P phase during prolonged operation. Furthermore, in a two-electrode configuration, the integrated Ni<sub>x</sub>P/MoS<sub>x</sub>||NiFe-LDH electrolyzer delivers low cell voltages of 1.46 and 1.61 V at 20 and 100 mA cm<sup>-2</sup>, respectively (Fig. S14), demonstrating efficient overall water splitting and practical applicability under alkaline conditions.

To elucidate the origin of the enhanced catalytic activity, operando EIS combined with kinetic isotope effect (KIE) analysis was performed. Nyquist plots reveal a pronounced suppression of the high-frequency semicircle for Ni<sub>x</sub>P/MoS<sub>x</sub> relative to pristine MoS<sub>x</sub> (Fig. 3a,b), indicating significantly reduced charge-transfer resistance and accelerated interfacial kinetics. Consistently, Bode phase analysis (Fig. 3c) shows faster surface relaxation dynamics and more efficient charge dissipation for Ni<sub>x</sub>P/MoS<sub>x</sub> under increasing cathodic bias. Quantitative fitting using an Armstrong–Henderson equivalent circuit (Fig. 3d) confirms substantially lower R<sub>ct</sub> values for Ni<sub>x</sub>P/MoS<sub>x</sub> compared to



pristine MoS<sub>x</sub> (Fig. S15a). Concurrently, an increase in the inverse adsorption resistance ( $1/R_{ad}$ ) and adsorption pseudo-capacitance ( $C_{ad}$ ) is observed (Fig. S15b,c), reflecting accelerated hydrogen adsorption/desorption kinetics and increased surface coverage of H\* intermediates.<sup>43,44</sup> All extracted fitting parameters are summarized in Table S4. EIS-derived Tafel analysis ( $\log(R_{ad})$  vs  $\eta$ )<sup>45</sup> yields a reduced slope for Ni<sub>x</sub>P/MoS<sub>x</sub> ( $\approx 97$  mV dec<sup>-1</sup>) compared to pristine MoS<sub>x</sub> ( $\approx 126$  mV dec<sup>-1</sup>) (Fig. 3e), indicating facilitated proton-electron transfer and a deviation from purely Volmer-limited behavior. This interpretation is further supported by KIE measurements (Fig. 3f), which show moderate  $J_{H_2O}/J_{D_2O}$  values ( $\approx 1.2$ – $1.5$ ) near the HER onset. Such values are consistent with a quasi-equilibrated Volmer step, suggesting that water dissociation is no longer the sole rate-determining step. Collectively, the operando EIS and KIE analyses demonstrate that Ni<sub>x</sub>P modification effectively alleviates the kinetic bottleneck associated with water dissociation, promoting a transition from a Volmer-limited pathway to post-Volmer kinetics governed by accelerated hydrogen adsorption/desorption dynamics. This synergistic enhancement of charge-transfer and surface reaction kinetics provides a mechanistic basis for the observed activity improvement and explains the inversion of conventional morphology–activity relationship.

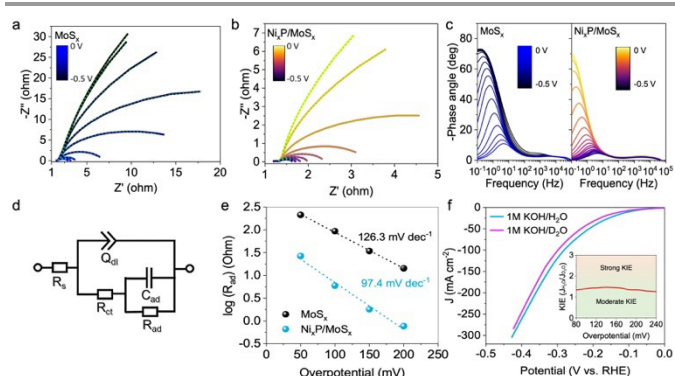


**Fig. 3.** Operando EIS Nyquist plots of (a) MoS<sub>x</sub> and (b) Ni<sub>x</sub>P/MoS<sub>x</sub> recorded over a frequency range of 100 kHz to 0.1 Hz at applied potentials from 0 to  $-0.5$  V vs RHE (0.05 V increments). The dotted lines are fits to the data. (c) Corresponding operando Bode phase plots in 1.0 M KOH. (d) Armstrong-Henderson equivalent circuit model used for fitting the EIS data. (e) EIS-derived Tafel-like plots for MoS<sub>x</sub> and Ni<sub>x</sub>P/MoS<sub>x</sub>. (f) LSV polarization curves of Ni<sub>x</sub>P/MoS<sub>x</sub> measured in 1.0 M KOH/H<sub>2</sub>O and 1.0 M KOH/D<sub>2</sub>O. Inset: corresponding kinetic isotope effect (KIE), indicating a moderate isotope effect.

In summary, Ni<sub>x</sub>P surface modification fundamentally reshapes the activity landscape of MoS<sub>x</sub> electrocatalysts via morphology-dependent interfacial coupling. Although polycrystalline MoS<sub>x</sub> nanosheets show higher intrinsic activity, Ni<sub>x</sub>P incorporation reverse this trend, rendering the amorphous–amorphous Ni<sub>x</sub>P/MoS<sub>x</sub> interface the most active ( $\eta_{10} = 96$  mV, Tafel slope = 67.5 mV dec<sup>-1</sup>). Operando electrochemical measurements and kinetic isotope effect analysis reveal that interfacial electronic coupling enhances charge-transfer efficiency and hydrogen adsorption kinetics, enabling a transition beyond a Volmer-limited mechanism. The Ni<sub>x</sub>P/MoS<sub>x</sub> catalyst also exhibits excellent durability and efficient overall water splitting (1.46 V at 20 mA cm<sup>-2</sup>), highlighting the critical role of amorphous interfaces in catalyst design.

## Authors contributions

I. Vamvasakis: data curation, methodology and analysis, writing original draft; A. Grammenos: investigation, synthesis, characterization, writing; G.S. Armatas: funding acquisition, conceptualization, general supervision, writing, review and editing.

## Data availability

The data supporting the findings of this study are available within the article and its Electronic Supplementary Information (ESI). Supplementary information: detailed experimental methods, synthesis procedures, and catalytic and spectroscopic characterization data.

## Conflicts of interest

There are no conflicts to declare.

## Acknowledgements

This study was carried out within the framework of the National Recovery and Resilience Plan Greece 2.0 (Award Number TAEDR-0535821), funded by the European Union – NextGenerationEU.

## References

- G. Squadrito, G. Maggiorini and A. Nicita, *Renew. Energy*, 2023, **216**, 119041.
- W. Sheng, H. A. Gasteiger and Y. Shao-Horn, *J. Electrochem. Soc.*, 2010, **157**, B1529.
- W. Sheng, M. Myint, J. G. Chen and Y. Yan, *Energy Environ. Sci.*, 2013, **6**, 1509–1512.
- J. Durst, A. Siebel, C. Simon, F. Hasché, J. Herranz and H. A. Gasteiger, *Energy Environ. Sci.*, 2014, **7**, 2255–2260.
- N. Mahmood, Y. Yao, J. W. Zhang, L. Pan, X. Zhang and J. J. Zou, *Adv. Sci.*, 2018, **5**, 1700464.
- M. Zeng and Y. Li, *J. Mater. Chem. A*, 2015, **3**, 14942–14962.
- X. Zou and Y. Zhang, *Chem. Soc. Rev.*, 2015, **44**, 5148–5180.
- B. Hinnemann, P. G. Moses, J. Bonde, K. P. Jørgensen, J. H. Nielsen, S. Horch, I. Chorkendorff and J. K. Nørskov, *J. Am. Chem. Soc.*, 2005, **127**, 5308–5309.
- D. Merki, S. Fierro, H. Vrubel and X. Hu, *Chem. Sci.*, 2011, **2**, 1262–1267.
- R. J. Toh, Z. Sofer, J. Luxa, D. Sedmidubský and M. Pumera, *Chem. Commun.*, 2017, **53**, 3054–3057.
- M. D. Patel, J. Zhang, J. Park, N. Choudhary, J. M. Tour and W. Choi, *Mater. Lett.*, 2018, **225**, 65–68.
- Q. Zhou, X. Luo, Y. Li, Y. Nan, H. Deng, E. Ou and W. Xu, *Int. J. Hydrogen Energy*, 2020, **45**, 433–442.
- C. Niu, H. Song, Y. Chang, W. Hou, Y. Li, Y. Zhao, Y. Xiao and G. Han, *J. Alloys Compd.*, 2022, **900**, 163509.
- Y. Li, Y. Yu, Y. Huang, R. A. Nielsen, W. A. Goddard, Y. Li and L. Cao, *ACS Catal.*, 2014, **5**, 448–455.
- T. F. Jaramillo, K. P. Jørgensen, J. Bonde, J. H. Nielsen, S. Horch and I. Chorkendorff, *Science*, 2007, **317**, 100–102.
- J. Kibsgaard, Z. Chen, B. N. Reinecke and T. F. Jaramillo, *Nat. Mater.*, 2012, **11**, 963–969.



- 17 E. D. Koutsouroubi, I. Vamvasakis, M. G. Minotaki, I. T. Papadas, C. Drivas, S. A. Choulis, G. Kopidakis, S. Kennou and G. S. Armatas, *Appl. Catal. B*, 2021, **297**, 120419.
- 18 F. Zakerian, M. Fathipour, R. Faez and G. Darvish, *J. Theo. Appl. Phys.*, 2019, **13**, 55–62.
- 19 Y. Zhou, C. Li, Y. Zhang, L. Wang, X. Fan, L. Zou, Z. Cai, J. Jiang, S. Zhou, B. Zhang, H. Zhang, W. Li and Z. Chen, *Adv. Funct. Mater.*, 2023, **33**, 2304302.
- 20 P. Man, S. Jiang, K. H. Leung, K. H. Lai, Z. Guang, H. Chen, L. Huang, T. Chen, S. Gao, Y. K. Peng, C. S. Lee, Q. Deng, J. Zhao and T. H. Ly, *Adv. Mater.*, 2024, **36**, 2304808.
- 21 X. Zhang and Y. Liang, *Adv. Sci.*, 2018, **5**, 1700644.
- 22 M. Kim, M. A. R. Anjum, M. Lee, B. J. Lee and J. S. Lee, *Adv. Funct. Mater.*, 2019, **29**, 1809151.
- 23 M. S. Metaxa, I. Vamvasakis, G. Kopidakis, G. Kioseoglou and G. S. Armatas, *Chem. Eng. J.*, 2025, **525**, 170118.
- 24 M. S. Metaxa, I. Vamvasakis and G. S. Armatas, *Small*, 2025, **22**, e13136.
- 25 M. S. Metaxa, I. Vamvasakis and G. S. Armatas, *Energy Environ. Mater.*, 2026, **9**, e70187.
- 26 P. Liu and J. A. Rodriguez, *J. Am. Chem. Soc.*, 2005, **127**, 14871–14878.
- 27 E. J. Popczun, J. R. McKone, C. G. Read, A. J. Biacchi, A. M. Wiltrout, N. S. Lewis and R. E. Schaak, *J. Am. Chem. Soc.*, 2013, **135**, 9267–9270.
- 28 S. Bra, I. Vamvasakis, E. K. Andreou, G. Vailakis, G. Kopidakis and G. S. Armatas, *Int. J. Hydrogen Energy*, 2023, **48**, 25300–25314.
- 29 N. Jiang, B. You, M. Sheng and Y. Sun, *ChemCatChem*, 2016, **8**, 106–112.
- 30 D. H. Song, D. Hong, Y. K. Kwon, H. W. Kim, J. Shin, J. Shin, H. M. Lee and E. A. Cho, *J. Mater. Chem. A*, 2020, **8**, 12069–12079.
- 31 A. B. Silva, M. Medina, L. A. Goulart and L. H. Mascaro, *Electrochim. Acta*, 2024, **475**, 143679.
- 32 G. Q. Han, X. Li, J. Xue, B. Dong, X. Shang, W. H. Hu, Y. R. Liu, J. Q. Chi, K. L. Yan, Y. M. Chai and C. G. Liu, *Int. J. Hydrogen Energy*, 2017, **42**, 2952–2960.
- 33 S. Hu, Q. Cao, H. Yao, Y. Jia and X. Guo, *ChemCatChem*, 2024, **16**, e202301420.
- 34 E. A. Ponomarev, M. Neumann-Spallart, G. Hodes and C. Lévy-Clément, *Thin Solid Films*, 1996, **280**, 86–89.
- 35 S. Subramaniam, S. Bharatan, S. Muthusamy and S. Sivaprakasam, *Coatings*, 2025, **15**, 146.
- 36 K. Gołasa, M. Grzeszczyk, R. Bozek, P. Leszczyński, A. Wyszomółek, M. Potemski and A. Babiński, *Solid State Commun.*, 2014, **197**, 53–56.
- 37 Z. Bojarska, M. Mężydło, M. Mazurkiewicz-Pawlicka and Ł. Makowski, *Appl. Sci.*, 2022, **12**, 11293.
- 38 N. Moses Badlyan, N. Pettinger, N. Enderlein, R. Gillen, X. Chen, W. Zhang, K. C. Knirsch, A. Hirsch and J. Maultzsch, *Phys. Rev. B*, 2022, **106**, 104103.
- 39 M. Chen, D. Liu, Y. Chen, D. Liu, X. Du, J. Feng, P. Zhou, B. Zi, Q. Liu, K. H. Lo, S. Chen, S. Wang, W. F. Ip and H. Pan, *Appl. Mater. Today*, 2022, **26**, 101343.
- 40 M. Moloudi, A. Noori, M. S. Rahmanifar, M. F. El-Kady, E. Mousali, N. B. Mohamed, X. Xia, Y. Zhang, A. Vinu, M. Vincent, D. Kowalski, R. B. Kaner and M. F. Mousavi, *Chem. Sci.*, 2025, **16**, 9484–9500.
- 41 C. H. Lee, J. M. Yun, S. Lee, S. M. Jo, K. Eom, D. C. Lee, H. I. Jho and T. F. Fuller, *Sci. Rep.*, **7**, 41190-. DOI: 10.1039/D6CC01893A
- 42 J. Kibsgaard, T. F. Jaramillo and F. Besenbacher, *Nat. Chem.*, 2014, **6**, 248–253.
- 43 N. Krstajić, M. Popović, B. Grgur, M. Vojnović and D. Šepa, *J. Electroanal. Chem.*, 2001, **512**, 16–26.
- 44 E. A. Franceschini, G. I. Lacconi and H. R. Corti, *Electrochim. Acta*, 2015, **159**, 210–218.
- 45 Y. Zhu, M. Klingenhof, C. Gao, T. Koketsu, G. Weiser, Y. Pi, S. Liu, L. Sui, J. Hou, J. Li, H. Jiang, L. Xu, W. H. Huang, C. W. Pao, M. Yang, Z. Hu, P. Strasser and J. Ma, *Nat. Commun.*, 2024, **15**, 1447.



## Data availability statements

The data supporting the findings of this study are available within the article and its Electronic Supplementary Information (ESI). Supplementary information: detailed experimental methods, synthesis procedures, and catalytic and spectroscopic characterization data.

